Nanoscale

PAPER

View Article Online
View Journal | View Issue

Cite this: *Nanoscale*, 2025, **17**, 26923

Fabrication and assessment of *n*-eicosane/poly(stearylmethacrylate-*co*-butylacrylate) nanocapsules: impact of long alkyl polymer chains on thermal performance and stability

Gunjan Varshney, [a] Raminder Kaur *[b] and Mohammad Zulfequar [c]

The objective of this study is to develop, characterise, and analyse thermal energy storage (TES) properties of *n*-eicosane/poly(stearylmethacrylate-*co*-butylacrylate) [ESE/P(SMA-*co*-BA)], a novel nanoencapsulated phase change material (NPCM). The NPCMs were produced *via* mini-emulsion polymerisation of a polymer shell, poly(stearylmethacrylate-*co*-butylacrylate) [P(SMA-*co*-BA)], around *n*-eicosane [ESE], which served as the core material. The thermal behaviour and thermal stability of ESE/P(SMA-*co*-BA) were determined using differential scanning calorimetry (DSC) and thermogravimetric analysis (TGA). According to DSC results, ESE/P(SMA-*co*-BA) has melting and crystallisation temperatures of 37.4 °C and 25.1 °C and latent heat values of 224.6 J g^{-1} and 191.7 J g^{-1}, respectively. The ESE/P(SMA-*co*-BA) nanocapsules exhibited an effective encapsulation efficiency (87.2%), encapsulation ratio (93.6%), and excellent thermal storage capacity (93.1%). The TGA study revealed the exceptionally good thermal stability of ESE/P(SMA-*co*-BA), with degradation in two stages. The chemical structure and crystallinity of the prepared ESE/P(SMA-*co*-BA) were verified using Fourier transform infrared (FTIR) spectroscopy and powder X-ray diffraction (PXRD) analysis. The results obtained from field emission scanning electron microscopy (FE-SEM), transmission electron microscopy (TEM), and polarized optical microscopy (POM) indicated that the synthesized ESE/P(SMA-*co*-BA) had a spherical morphology with a mean particle diameter of 195.3 nm, as determined by particle size distribution (PSD) analysis. This research highlighted a novel technique for fabricating phase transition materials for TES, which can be used in a variety of applications, including food storage containers, smart textiles, and building, medical and electronic materials.

Received 2nd October 2025,
Accepted 28th October 2025

DOI: 10.1039/d5nr04183j

rsc.li/nanoscale

1. Introduction

Energy from various renewable sources, including solar, biomass, geothermal and tidal power, has garnered immense attention in recent years as a means of curbing environmental pollution and promoting sustainable development.[1,2] Thermal energy accounts for about 60%–70% of global energy consumption, though it is quite challenging to convert it into mechanical work or electricity due to high entropy and significant losses. Excessive waste and intermittent thermal energy supply typically result in low energy utilisation efficiency and create a mismatch between supply and demand. Since the last century, numerous thermal energy storage (TES) technologies have been developed to enhance utilisation efficiency and accomplish the requisite regulation of thermal energy.[3,4] Latent heat storage based on phase change materials (PCMs) is one of the most actively explored TES technologies, owing to its operational simplicity as well as substantial energy storage density at constant temperature. PCMs are substances capable of storing and releasing thermal energy during the phase transition process within a specific temperature range. PCMs are becoming more prevalent in a variety of applications, including automotive battery energy management systems,[5] thermal-regulated textiles,[6] solar energy storage systems,[7] industrial waste heat utilization[8] and energy-efficient buildings.[9] PCMs are divided into three categories based on their state aggregations: solid–solid, solid–liquid, and liquid–gas. Among these three categories, solid–liquid PCMs are the most promising for TES and thermal management due to their high energy storage capacity, isothermal behaviour, and minimal volume variation during phase transitions.[10]

The direct use of PCMs with solid-to-liquid phase transitions in TES systems is undesirable because of their

[a]*Research Scholar, Discipline of Polymer Science and Chemical Technology, Department of Applied Chemistry, Delhi Technological University (Formerly Delhi College of Engineering), Delhi-110042, India*
[b]*Associate Professor, Discipline of Polymer Science and Chemical Technology, Department of Applied Chemistry, Delhi Technological University (Formerly Delhi College of Engineering), Delhi-110042, India. E-mail: rkwalia14@gmail.com*
[c]*Professor, Department of Physics, Jamia Millia Islamia, Jamia Nagar, New Delhi, 110025, India*

flow/leakage issues during phase transitions and their poor thermal conductivity, which limits their utility for many applications.[11,12] Leakage can lead to negative consequences, such as packing contamination or electronic device failure due to phase change. On the other hand, low thermal conductivity means that PCMs can store and release energy at a very low rate, making them unsuitable for a variety of applications. These constraints impede the commercial use of PCMs to meet energy demands and other thermal applications for a growing population. To address these concerns, PCMs should be encapsulated in an appropriate polymer shell.[13] Encapsulated PCMs have significant advantages over bulk counterparts, including increased thermal stability, compatibility with various matrices, and ease of handling. Several encapsulation methods have been investigated, including suspension polymerisation,[14] spray drying,[15] and interfacial polymerisation.[16] Each approach has benefits and drawbacks, based on the desired shell material, capsule size and encapsulation efficiency.

Zhang *et al.*[17] employed an *in situ* polymerisation technique to produce nanoencapsulated PCM (NPCM) with a paraffin wax core and melamine formaldehyde resin shell. Their NPCM had melting and freezing temperatures of around 49 °C and 54 °C, with latent heats of 107.4–135.3 J g^{-1} and 109.8–133.1 J g^{-1}, respectively. NPCM achieved a maximum encapsulation efficiency (E_{ES}) of 75%. Ghulam *et al.*[18] synthesized an NPCM based on an *n*-eicosane (ESE) core and inorganic shell *via* the sol–gel method. Sodium silicate and tetraethyl-orthosilicate were used as inorganic silica precursors under different conditions to enhance thermal stability and phase change properties. The obtained nanocapsules exhibited good properties with high encapsulation rates and thermal stability when prepared at pH 2.90–3.00, but showed very poor E_{ES} and enthalpies when prepared under pH 2.9. Sari *et al.*[19] aimed to prepare micro/nano-encapsulated paraffin eutectic mixtures (PEMs) with a poly(methylmethacrylate) (PMMA) shell. Using emulsion polymerisation, four new PMMA-based micro/nanocapsules were prepared: PMMA/(C19–C18), PMMA/(C17–C24), PMMA/(C19–C24), and PMMA/(ESE–C24). The DSC results showed that the encapsulated PEMs with the highest PEM had a high latent heat storage capacity of 86–169 J g^{-1} and a melting temperature range of 20 °C–36 °C. Zhou *et al.*[20] used the surfactant-free emulsion polymerisation approach to nanoencapsulate butyl stearate and C18 binary cores within a nano-TiO_2-modified polyacrylate hybrid shell. The derived nanocapsules demonstrated a remarkable latent heat storage performance, with an E_{ES} of 61.5%. Rezvanpour *et al.*[21] developed micro-nanocapsules with PMMA as the shell and ESE as the core in a weight ratio of 1 : 1 using the mini-emulsion polymerisation process. The ESE/PMMA micro-nanocapsules have melting and freezing temperatures of 34.7 °C and 32.9 °C, as well as latent heats of 124.7 J g^{-1} and −119.1 J g^{-1}. Furthermore, the encapsulation ratio (E_R) was determined to be 62%. Nikoonahad *et al.*[22] applied the "sol–gel" method to fabricate unique core–shell nanostructures with a capric acid core and a highly stable TiO_2 shell. Their findings indicated that the synthesized nanocapsules had a nearly spherical shape, with a mean diameter of 100–500 nm. The synthesized nanocapsules melt at 31.1 °C with a latent heat of 88.8 J g^{-1} and solidify at 28.9 °C with a latent heat of 84.2 J g^{-1}. The optimal E_R of 56.67% was achieved using a CA/TNBT mass ratio of 8.1 and a pH of 2.6. Lan *et al.*[23] adopted a mini-emulsion polymerisation approach to prepare nanocapsules composed of octadecane and SiO_2/BN shell. Their approach resulted in an increase in thermal conductivity to 0.9 W m^{-1} K^{-1}, yielding an E_R greater than 50%.

From the literature data, it is evident that the nanoencapsulation of ESE PCMs with a P(SMA-*co*-BA) shell has not been explored to date. This study employs mini-emulsion polymerisation to synthesise ESE/P(SMA-*co*-BA) nanocapsules with ESE as the core material. ESE was selected as the encapsulating PCM due to its ideal melting point of 35.5 °C, high latent heat capacity, and relevance for applications, such as thermo-regulated foams, thermal insulation, textiles, fibres and building materials. To achieve optimal encapsulation, P(SMA-*co*-BA) was selected as the shell material, with polystearylmethacrylate (PSMA) serving as the main polymer shell and polybutylacrylate (PBA) as a copolymer. The current study expands on our earlier research on microencapsulation with a polystyrene shell by investigating nanoencapsulation with a PSMA shell to improve PCM thermal stability.[24] The rigid aromatic structure of the polystyrene shell resulted in significantly lower thermal stability, while the long alkyl polymer chain shell optimises both thermal stability and interfacial compatibility. Furthermore, a reduced particle size in nanoencapsulation raises the surface area-to-volume ratio, improving heat transfer rates and resolving the problem of low thermal conductivity. Nanoencapsulation enhances the dispersion of PCMs, reduces leakage, and offers superior protection against environmental factors. Additionally, the structural alterations caused by long alkyl polymer chains promote phase change behaviour, augment durability, and extend operational efficiency, rendering nanoencapsulation a more effective and reliable solution for advanced TES applications.

A key innovation of this study is the inclusion of PSMA, which incorporates long alkyl polymer chains into the shell structure, substantially enhancing the compatibility, stability, and thermal regulation qualities of the nanocapsules. These long alkyl chains facilitate the formation of crystalline regions within the polymer matrix, which affects the thermal transitions of NPCMs. Furthermore, the highly hydrophobic nature of these long chains reduces moisture absorption, resulting in enhanced thermal stability and extended endurance across a variety of environmental conditions. In addition to the structural benefits of PSMA, PBA serves as a copolymer, boosting mechanical flexibility and toughness and diminishing the chances of nanocapsule rupture during the heating cycle. Its elastomeric nature reinforces the polymer shell, resulting in high E_{ES} and long-term durability. The amalgamation of PSMA's crystalline long alkyl chains and PBA's flexibility yields a strong, versatile encapsulation system with superior thermal stability, mechanical resilience, and controlled release pro-

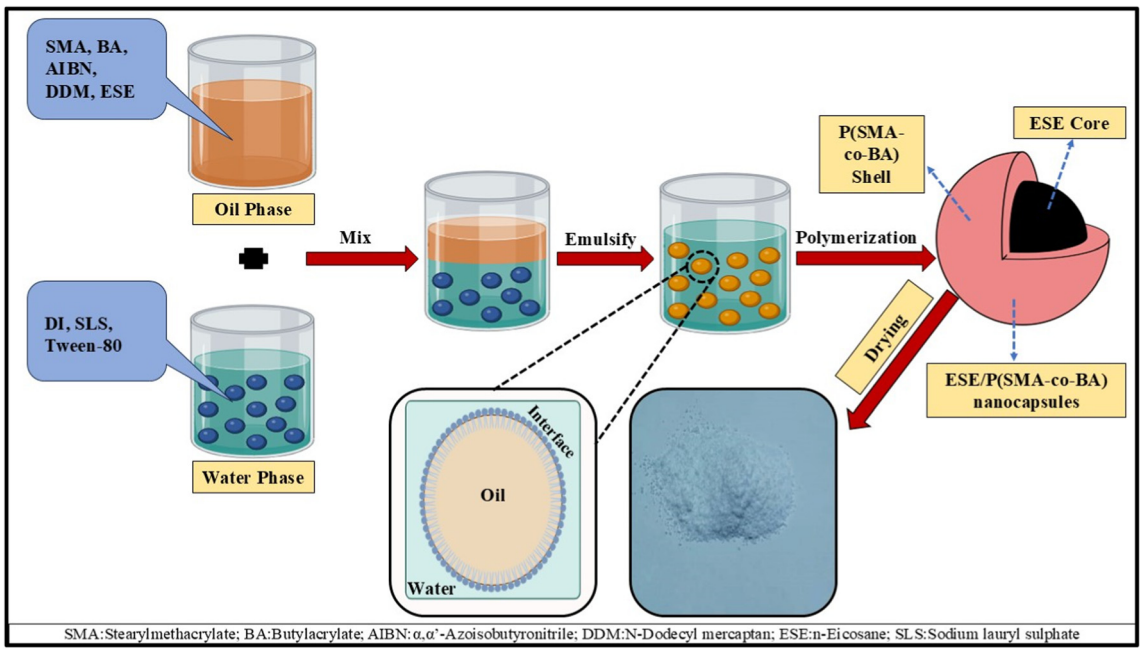

Fig. 1 An illustration of the experimental approach for ESE/P(SMA-*co*-BA) synthesis.

perties. The thermal and chemical properties, overall thermal stability, surface morphology and particle size distribution of the synthesised ESE/P(SMA-*co*-BA) nanocapsules were also investigated. The combination of long alkyl polymer chains and an elastomeric copolymer shell results in a novel, highly efficient encapsulation strategy, making these nanocapsules suitable for a wide range of applications, including energy-efficient building materials, electronic cooling systems and textiles.

2. Material and methodology

2.1. Materials

The monomer, stearyl methacrylate (SMA, 98%, Sigma Aldrich), was rinsed three times with an aqueous solution containing 10% sodium hydroxide, followed by Milli-Q water. The hydrophobic co-monomer, butyl acrylate (BA, 99%, Central Drug House), was used without purification. *n*-Eicosane (ESE, 99%, TCI Chemicals) was used as the core material. Sodium lauryl sulphate (SLS, Sisco Research Laboratories) and Tween-80 (Thomas Baker Chemicals) were used as emulsifiers. α,α′-Azoisobutyronitrile (AIBN, Spectrochemicals) was employed as an initiator. *N*-Dodecyl mercaptan (DDM, 98%, Loba Chemie) was used as the chain transfer agent (CTA). All reactions were carried out using Milli-Q water.

2.2. Methodology

ESE/P(SMA-*co*-BA) nanocapsules were produced using the mini-emulsion polymerisation process. Typically, an oily mixture is formed by combining 12 mL ESE, 12 mL SMA, 0.2 mL BA, 0.1 ml DDM and 0.1 g AIBN. An aqueous medium was prepared by the addition of 144 mL Milli-Q water with 0.2 g SLS and 0.2 mL Tween-80 composite surfactants. Afterwards, the oil phase was steadily mixed into the aqueous phase and stirred at 5000 rpm for 30 min. Miniemulsification was performed for 10 min by sonifying the emulsion at 75% amplitude with a sonifier (Model UP400St, Hielscher, Germany). To prevent thermal polymerisation during sonification, the emulsion was immersed in an ice bath. Afterwards, the emulsion was transferred to a 500 ml two-neck round-bottom flask fitted with a stirrer and condenser. To eliminate the oxygen, nitrogen purging was done for 30 min. The reaction was conducted for 12 h under the same reaction conditions, with the flask submerged in a water bath at 85 °C. Following the reaction, the latex temperature was gradually brought down to room temperature. Fig. 1 displays a schematic illustration of the proposed experimental approach for producing ESE/P(SMA-*co*-BA) nanocapsules.

3. Characterization of ESE/P(SMA-*co*-BA)

Differential scanning calorimetry (DSC8000, PerkinElmer) was used to analyse thermal characteristics, including melting point, crystallisation point, and enthalpies related to heating and cooling processes. Each sample, weighing approximately 5.0 mg, was placed into an aluminium crucible. Each sample underwent three heating/cooling cycles at temperatures ranging from −10 °C to 70 °C. The furnace temperature was consistently ramped at 10 °C min^{-1} with a constant N_2 flow rate. The ESE/P(SMA-*co*-BA) samples were investigated thrice, and their average E_{ES} and TES characteristics were recorded.

The synthesised ESE/P(SMA-*co*-BA) was subjected to thermogravimetric analysis (TGA) using a thermogravimetric analyser (Pyris Diamond TGA, PerkinElmer). The sample was placed in a platinum crucible and heated from 30 °C to 800 °C in a furnace under an inert environment of N_2 at a steady rate of 10 °C min^{-1}. As the temperature rises, the sample shows mass loss, primarily due to the evaporation of volatile components and subsequently (at very high temperatures) thermal breakdown. The change in sample mass was measured in relation to temperature. To assess the thermal reliability of ESE/P(SMA-*co*-BA), an accelerated thermal cycling test (100 melting/crystallizing cycles) was performed.[1,25–27]

A Spectrum Two, PerkinElmer Fourier-transform infrared spectrometer (FT-IR) equipped with a KBr disk was utilized to investigate the interactions of functional groups and chemical bonds in the prepared ESE/P(SMA-*co*-BA) within the range of 500–4000 cm^{-1}. A powder X-ray diffractometer (PXRD) with Cu Kα radiation (Smart Lab 3 kW, Rigaku) was used for crystallographic investigation of the synthesised NPCM. The XRD patterns were recorded at 298 K within the 2θ range of 10° to 80° with step size of 0.02°, and a scanning rate of 1.0 s per step. The surface morphology and shape of ESE/P(SMA-*co*-BA) were explored with the help of field emission scanning electron microscopy (FE-SEM, Thermoscientific Apreo 2S) and transmission electron microscopy (TEM, Morgagni 268D). Using the dynamic light scattering method (DLS, Malvern Zetasizer Nano ZS, UK), particle size distribution (PSD) and the average diameter of the prepared nanocapsules were assessed. Three scans were performed for each observation to record the PSD and average particle size of the nanocapsules.

4. Results and discussion

4.1. Thermal performance of ESE/P(SMA-*co*-BA) nanocapsules

Fig. 2(a–d) depicts the DSC thermogram for the ESE and ESE/P(SMA-*co*-BA) samples throughout a temperature range of 5 °C to 100 °C, with a scanning rate of 10 °C min^{-1}. The DSC was used to assess the fundamental thermal properties, including melting and crystallisation temperatures, along with their associated latent heat values. It also describes the thermal behaviour of the material during phase transitions. Tables 1 and 2 display the experimental outcomes derived from the DSC analysis. The DSC plots of ESE and ESE/P(SMA-*co*-BA) exhibit both exothermic and endothermic peaks, and the shaded region shows the prominent peaks of the materials. The melting and crystallisation temperatures of ESE were

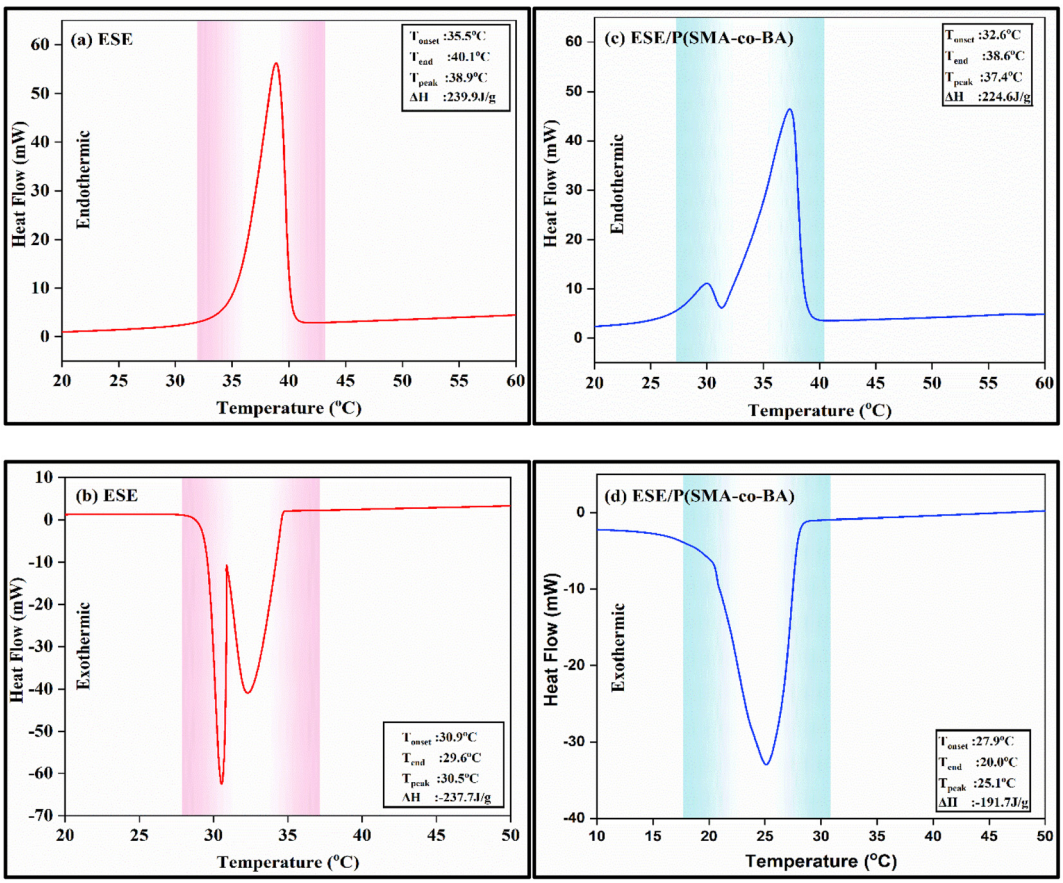

Fig. 2 DSC thermograms of the (a and b) pristine ESE and (c and d) synthesized ESE/P(SMA-*co*-BA) nanocapsules.

Table 1 DSC analysis results of the endothermic process in pure ESE and ESE/P(SMA-*co*-BA) nanocapsules

	Onset temperature	Peak temperature	Endset temperature	Latent heat of melting	
ESE	35.5 °C	38.9 °C	40.1 °C	239.9 J g^{-1}	Ref. 24
ESE/P(SMA-*co*-BA)	32.6 °C	37.4 °C	38.6 °C	224.6 J g^{-1}	Present study

Table 2 DSC analysis results of the exothermic process in pure ESE and ESE/P(SMA-*co*-BA) nanocapsules

	Onset temperature	Peak temperature	Endset temperature	Latent heat of crystallization	
ESE	30.9 °C	30.5 °C	29.6 °C	237.7 J g^{-1}	Ref. 24
ESE/P(SMA-*co*-BA)	27.9 °C	25.1 °C	20.0 °C	191.7 J g^{-1}	Present Study

determined from DSC thermograms and were found to be 38.9 °C and 30.5 °C, respectively. The observed latent heat of fusion was 239.9 J g^{-1}, while the latent heat of crystallisation was 237.7 J g^{-1} (Fig. 2(a) and (b)). The ESE/P(SMA-*co*-BA) nanocapsules exhibit a melting temperature of 37.4 °C, accompanied by a latent heat of 224.6 J g^{-1} and a crystallization temperature of 25.1 °C, with a latent heat of crystallization of 191.7 J g^{-1} (Fig. 2(c) and (d)). The observed decrease in latent heat is attributed to the presence of the P(SMA-*co*-BA) polymer shell.[28] The findings confirm that the synthesized ESE/P(SMA-*co*-BA) has remarkable heat storage capabilities and substantial potential for use in TES applications, including waste heat recovery, solar energy systems, building materials, smart textiles and thermo-responsive coatings.

4.1.1. Effect of long-alkyl SMA polymer shell crystallinity on the thermal behaviour of NPCMs. From Fig. 2, it was found that the DSC thermogram of pristine ESE shows a single sharp endothermic peak at 38.9 °C and two sharp exothermic peaks at 30.5 °C and 32.3 °C, respectively. On the contrary, the DSC thermogram of NPCMs shows dual endothermic peaks at 30 °C and 37.4 °C and a single exothermic peak at 25.1 °C. This drastic change is due to the dominant nature of the long alkyl side chains of methacrylate towards thermal transitions to a great extent.[29]

At a lower temperature, the first endothermic peak of the NPCMs is observed, which is associated with the melting of the crystalline stearyl side chains of PSMA from the polymer shell P(SMA-*co*-BA) (Fig. 3).[30–33] The long alkyl side chains in PSMA, a semi-crystalline polymer, can crystallise independently to form ordered domains within the polymer matrix. It is important to note that the primary methacrylate backbone remains intact when these side chains melt. Instead, this transition represents the thermal softening or reorganisation of the crystalline side-chain regions, which can occur without jeopardising the structural integrity of the enclosing shell.

The melting of ESE is represented by the second endothermic peak. This peak appears broader and slightly shifted compared to bulk ESE; this behaviour is ascribed to restricted molecular mobility, confinement effects, and interfacial interactions between the core and the shell.[34] These parameters alter the melting dynamics of PCM, resulting in a less abrupt transition.

In contrast to the two distinct crystallisation peaks observed in pure ESE, the NPCM displayed a single broad exothermic peak throughout the cooling cycle. The overlapping crystallisation events of the PSMA shell and the paraffin core, which occur in comparable temperature ranges, are most likely the cause of this combined peak.[35] The broad exothermic response is facilitated by the independent crystallisation of PSMA, which is stimulated by the reorganisation of its side chains, whereas the multi-step crystallisation of paraffin that is usually

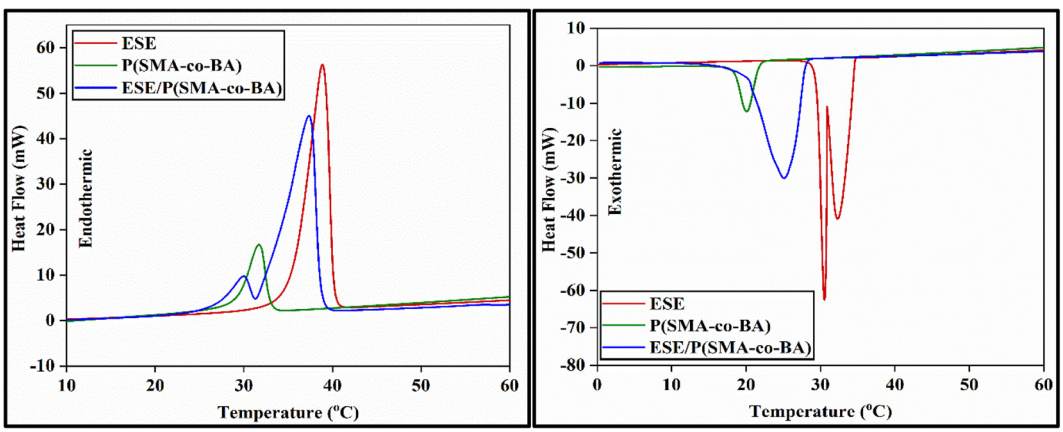

Fig. 3 Endothermic and exothermic DSC thermograms of the ESE, P(SMA-*co*-BA) and the prepared ESE/P(SMA-*co*-BA).

Table 3 Comparative study of the prepared NPCMs with the shorter and longer alkyl methacrylate polymer shells

Shell	PCM	PCM : shell	$\Delta H_{m\text{-EPCM}}$ (J g^{-1})	$\Delta H_{c\text{-EPCM}}$ (J g^{-1})	E_R/E_{ES} (%)	Ref.
PMMA	Paraffin	1 : 1	64.9	66.4	E_{ES} = 52.9	38
	ΔH_c: 122.4 J g^{-1}	3 : 4	62.3	63.9	50.9	
	ΔH_c: 125.7 J g^{-1}	3 : 5	62.2	64.4	50.0	
		1 : 2	60.3	61.7	48.1	
PMMA/SiO_2	Paraffin	—				39
	ΔH_m: 121.0 J g^{-1}	10.5 : 3	70.0	71.0	E_{ES} = 57.4	
	ΔH_c: 124.5 J g^{-1}	11.5 : 2	57.5	57.5	46.9	
		12.5 : 1	53.5	53.5	43.6	
		13.5 : 0	62.1	62.4	50.7	
PMMA	Nonadecane	2 : 1	43.6	49.4	—	40
	ΔH_m: 230.7 J g^{-1}	1 : 1	61.9	63.7	—	
	ΔH_c: 223.8 J g^{-1}	1 : 2	139.2	142.4	E_R = 60.3	
PMMA	ESE	1 : 1	124.7	119.1	E_R = 62	21
	ΔH_m: 202.5 J g^{-1}					
	ΔH_c: 193.4 J g^{-1}					
PBMA-*co*-DVB	Octadecane	(C_{18}) 1 : 1	87.9	90.5	E_{ES} = 41.2	41
	(C_{18})	(BS) 1 : 1	37.4	37.6	35.3	
	ΔH_m: 216.0 J g^{-1}	(C_{18} : BS = 1 : 1)				
	ΔH_c: 216.4 J g^{-1}	1 : 1	40.3	42.1	33.7	
	Butyl stearate	(C_{18} : BS = 1 : 1)				
	(BS)	2 : 1	93.1	91.9	71.3	
	ΔH_m: 104.0 J g^{-1}					
	ΔH_c: 108.1 J g^{-1}					
(i) P(BMA-*co*-BA)	Octadecane	1 : 1			E_{ES} =	42
	ΔH_m: 223.1 J g^{-1}		(i) 116.4	(i) 125.5	(i) 53.7	
(ii) P(BMA-*co*-BA-*co*-MAA)	ΔH_c: 227.1 J g^{-1}		(ii) 136.3	(ii) 130.0	(ii) 59.2	
(iii) P(BMA-*co*-MAA)			(iii) 144.3	(iii) 152.9	(iii) 66.0	
(iv) P(BMA-*co*-AA)			(iv) 141.5	(iv) 143.0	(iv) 63.2	
(i) PBMA (with DVB)	Octadecane	1 : 1			E_{ES} =	43
	ΔH_m: 223.1 J g^{-1}		(i) 107.1	(i) 109.4	(i) 48.1	
(ii) PBMA (with PETA)	ΔH_c: 227.1 J g^{-1}		(ii) 126.4	(ii) 123.7	(ii) 55.6	
PU/PBMA	Paraffin	1 : 1			E_{ES} =	44
(i) with Diethylenetriamine	ΔH_m: 166.0 J g^{-1}		(i) 106.0	(i) 95.7	(i) 61.3	
(ii) with Diethylenetriamine and Glycerol (1 : 1)	ΔH_c: 163.1 J g^{-1}		(ii) 145.2	(ii) 126.7	(ii) 82.6	
PLMA-*co*-DVB	Octadecane (C_{18})	(C_{18}) 1 : 1	67.7	67.2	E_{ES} = 31.2	41
	ΔH_m: 216.0 J g^{-1}	(BS) 1 : 1	34.3	30.7	30.6	
	ΔH_c: 216.4 J g^{-1}	(C_{18} : BS = 1 : 1)				
	Butyl stearate (BS)	1 : 1	36.4	27.6	24.7	
	ΔH_m: 104.0 J g^{-1}	(C_{18} : BS = 1 : 1)	80.3	81.1	62.2	
	ΔH_c: 108.1 J g^{-1}					
PLMA	Octadecane	1 : 1	118.0	108.9	E_{ES} = 50.4	45
	ΔH_m: 223.1 J g^{-1}		76.7	73.0	45.5	
	ΔH_c: 227.1 J g^{-1}					
	Paraffin					
	ΔH_m: 166.0 J g^{-1}					
	ΔH_c: 163.1 J g^{-1}					
(i) PU/PLMA	Paraffin	1 : 1			E_{ES} =	46
	ΔH_m: 192.2 J g^{-1}		(i) 102.7	(i) 99.3	(i) 52.6	
(ii) PU/PLMA (with TMP)	ΔH_c: 191.5 J g^{-1}		(ii) 127.6	(ii) 124.7	(ii) 65.8	
(iii) PU/PLMA (with PETA)			(iii) 132.3	(iii) 127.8	(iii) 67.8	
(i) PSMA (with PETA)	Octadecane	1 : 1			E_{ES} =	34
	ΔH_m: 223.1 J g^{-1}		(i) 82.6	(i) 80.7	(i) 36.3	
(ii) PSMA (with DVB)	ΔH_c: 227.1 J g^{-1}		(ii) 87.9	(ii)94.8	(ii) 40.6	
PSMA-*co*-DVB	Octadecane	(C_{18}) 1 : 1	85.9	99.1	E_{ES} = 42.8	41
	(C_{18})	(BS) 1 : 1	36.0	38.7	35.2	
	ΔH_m: 216.0 J g^{-1}	(C_{18} : BS = 1 : 1)				
	ΔH_c: 216.4 J g^{-1}	1 : 1	60.3	59.4	46.1	
	Butyl stearate	(C_{18} : BS = 1 : 1)				
	(BS)	2 : 1	86.3	90.1	68.0	
	ΔH_m: 104.0 J g^{-1}					
	ΔH_c: 108.1 J g^{-1}					
P(SMA-*co*-BA)	ESE	1 : 1	224.6	191.7	E_R = 93.6	This study
	ΔH_m: 239.9 J g^{-1}				E_{ES} = 87.2	
	ΔH_c: 237.7 J g^{-1}					

PMMA: polymethylmethacrylate; PBMA: polybutylmethacrylate; PLMA: polylaurylmethacrylate and PSMA: polystearylmethacrylate.

observed in its bulk form is limited by nano-confinement within the shell.[36,37] The produced NPCMs are compared with other encapsulated PCMs featuring shorter and longer alkyl polymer shells in Table 3.

4.1.2. Phase change performance. The phase-change temperatures and enthalpies of pristine ESE and ESE/P(SMA-*co*-BA) are obtained using DSC thermograms. The pristine ESE exhibits significantly elevated phase change enthalpies, as shown in Tables 1 and 2. This signifies that the ESE PCM possesses a substantial capacity for latent heat storage and can nearly discharge it as it changes phase. The encapsulation of ESE within the P(SMA-*co*-BA) shell significantly decreased the absolute phase change enthalpies of the nanocapsules. Due to the inert P(SMA-*co*-BA) shell, the latent heat may solely be stored by the phase-changeable ESE core. Consequently, the phase change enthalpies of the synthesized nanocapsules are significantly dependent on the loading of ESE within the nanocapsule. Two vital factors, namely the E_R and E_{ES}, are employed to describe the phase-change performance of NPCMs and can be derived from DSC data using eqn (1) and (2):[47,48]

$$E_R = \frac{\Delta H_{(m)[ESE/P(SMA\text{-}co\text{-}BA)]}}{\Delta H_{(m)ESE}} \times 100\% \quad (1)$$

$$E_{ES} = \frac{\Delta H_{(m)[ESE/P(SMA\text{-}co\text{-}BA)]} + \Delta H_{(c)[ESE/P(SMA\text{-}co\text{-}BA)]}}{\Delta H_{(m)ESE} + \Delta H_{(c)ESE}} \times 100\% \quad (2)$$

$\Delta H_{(m)ESE}$ and $\Delta H_{(m)[ESE/P(SMA\text{-}co\text{-}BA)]}$ denote the melting enthalpies of pristine ESE and NPCM, respectively; $\Delta H_{(c)ESE}$ and $\Delta H_{(c)[ESE/P(SMA\text{-}co\text{-}BA)]}$ represent the crystallization enthalpies of pristine ESE and NPCM, respectively. E_R indicates the ESE encapsulation within the nanocapsules, whereas the loading content refers to the dry weight percentage of the core material. It is comprehensible that not all nanocapsules can serve as PCMs, as phase transitions often do not transpire within small-sized nanocapsules due to the confinement of molecular motion. On the contrary, E_{ES} represents the effective performance of ESE inside the ESE/P(SMA-*co*-BA) nanocapsules for heat energy storage and thermal regulation. Furthermore, E_{ES} is inferred from the enthalpies associated with melting and crystallization.

The synthesized nanocapsules achieved an E_R of 93.6% and an E_{ES} of 87.2% at an ESE/PSMA mass ratio of 1 : 1. Furthermore, the thermal storage capacity (C_{es}) of the nanoencapsulated ESE may be ascertained using the findings obtained from DSC measurements by employing eqn (3):[49]

$$C_{es} = \frac{E_{ES}}{E_R} \times 100\% \quad (3)$$

The nanocapsules were prepared at an ESE/P(SMA-*co*-BA) mass ratio of 1 : 1 and have a C_{es} of 93.1%, suggesting that nearly all encapsulated ESE may efficiently store latent heat during the phase transition. The ESE has been configured to an appropriate shape and size, resulting in enhancing the capability of the material to store and release energy even at or beyond the phase transition temperature without undergoing any material deformation.

4.2. Thermal stability of ESE/P(SMA-*co*-BA) nanocapsules

The thermal stability and degradation pattern of ESE, P(SMA-*co*-BA) and NPCMs were analyzed using TGA and DTG. The thermograms are presented in Fig. 4. The pure ESE undergoes degradation in a singular phase, initiating mass loss at around 75 °C and completely losing its weight at 265 °C. This weight loss may be ascribed to the degradation of linear alkane chains. Due to ESE being a long-chain *n*-alkane with a comparatively low degradation temperature, the mass of pure ESE decreases significantly as the temperature increases.[24] Conversely, ESE/P(SMA-*co*-BA) demonstrated a two-phase deterioration pattern. The initial weight-loss stage (165.6 °C) likely results from the diffusion of *n*-alkane from the polymer shell, P(SMA-*co*-BA), which may evaporate or degrade as the temperature increases. The second weight-loss phase occurred at 299.4 °C due to the disintegration of the P(SMA-*co*-BA) shell.

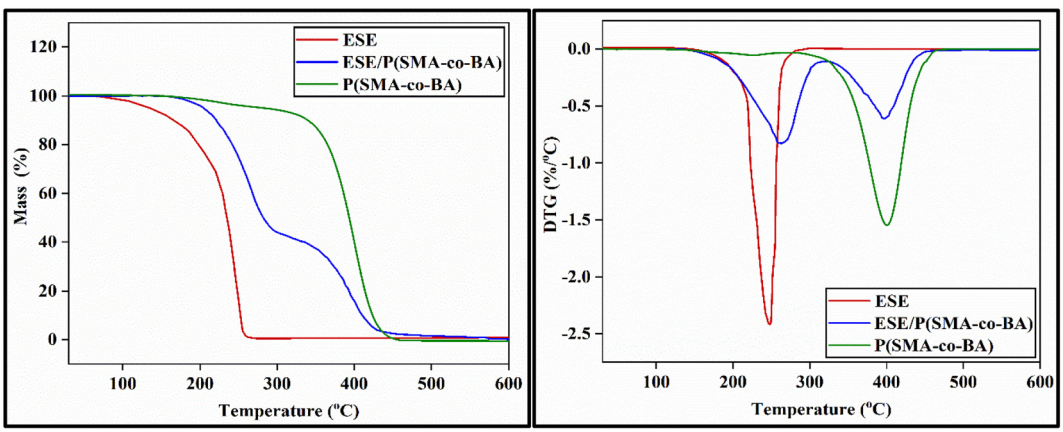

Fig. 4 TGA and DTG curves of ESE, P(SMA-*co*-BA) and ESE/P(SMA-*co*-BA) nanocapsules.

Table 4 Thermal properties of ESE/P(SMA-*co*-BA) with 100 heating and cooling cycles

No. of thermal cycling	Onset temperature	Peak temperature	Endset temperature	Latent heat of melting	Onset temperature	Peak temperature	Endset temperature	Latent heat of crystallization
0	32.6 °C	37.4 °C	38.6 °C	224.6 J g^{-1}	27.9 °C	25.1 °C	20.0 °C	191.7 J g^{-1}
100	32.6 °C	37.6 °C	38.8 °C	222.9 J g^{-1}	27.7 °C	25.2 °C	20.0 °C	189.5 J g^{-1}

The remaining synthetic NPCM entirely dissipates at 600 °C.[34,41] The TGA data for ESE, P(SMA-*co*-BA) and NPCMs were confirmed by the DTG curves. Furthermore, it is apparent that the initial weight-loss temperature of ESE/P(SMA-*co*-BA) was significantly elevated by 90.6 °C in comparison to the pure PCM. This outcome demonstrated that the P(SMA-*co*-BA) shell effectively protects the core material and inhibits ESE leakage from the nanocapsules.

4.3. Thermal reliability of ESE/P(SMA-*co*-BA) nanocapsules

A thermal cycling test was conducted to examine the irreversibility of energy storage and the chemical stability of NPCMs

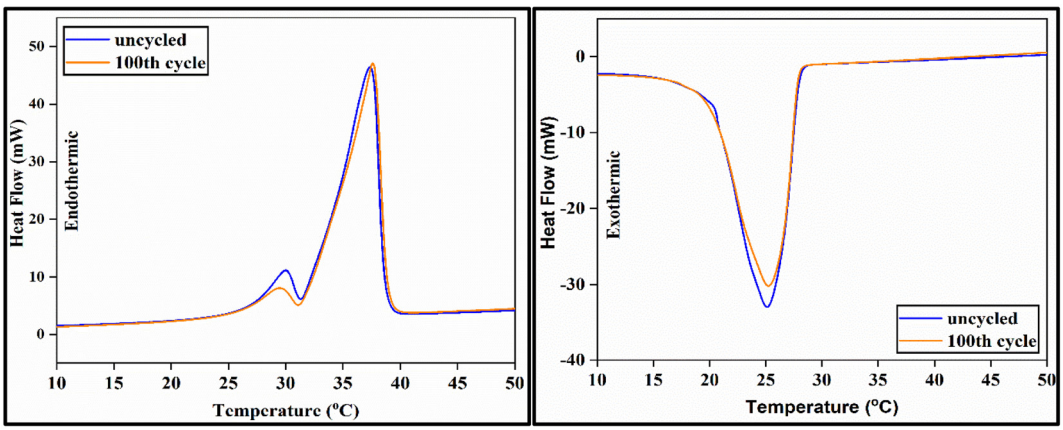

Fig. 5 DSC thermograms of ESE/P(SMA-*co*-BA) before and after 100 cycles.

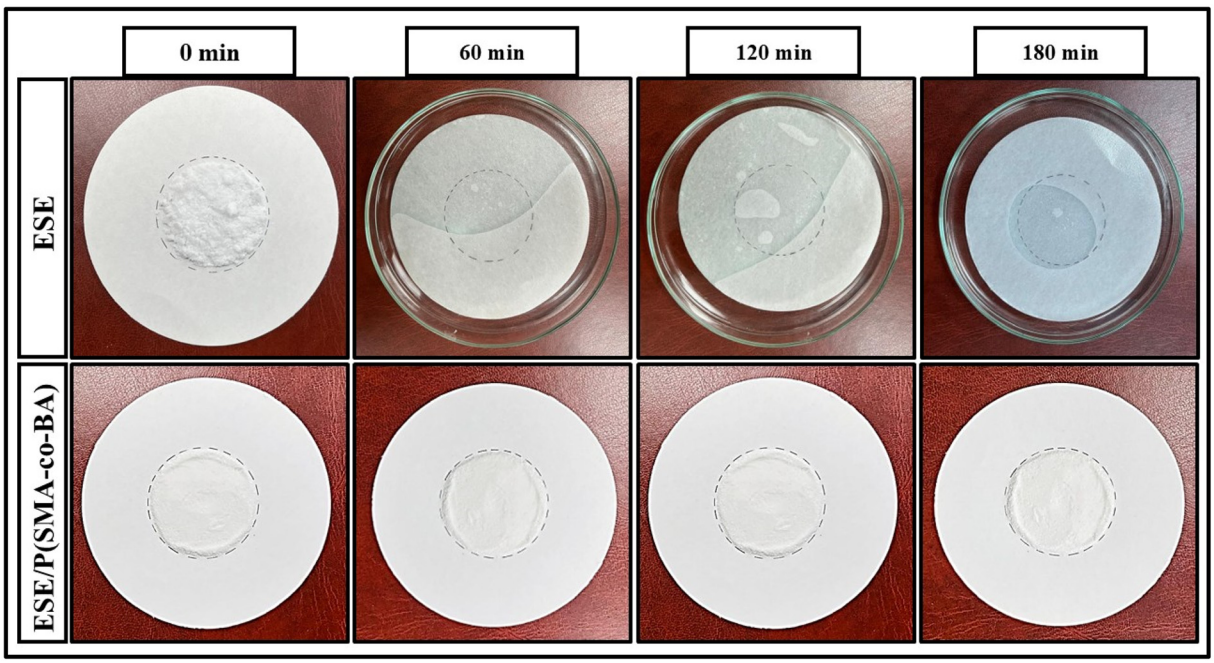

Fig. 6 Photographic images of ESE and ESE/P(SMA-*co*-BA) from the diffusion-oozing circle test.

after numerous cycles of heating and cooling. ESE/P (SMA-*co*-BA) was subjected to 100 thermal cycling tests. The thermal properties are listed in Table 4, and the DSC thermograms before and after thermal cycling are shown in Fig. 5. The melting and crystallisation temperatures of the nanocapsules did not alter significantly after 100 cycles, as shown in Fig. 5 and Table 4. On the other hand, the latent heat value of melting and crystallization decreased by 1.7 and 2.2 J g^{-1}, respectively. The results demonstrate that the DSC curves before and after the thermal cycles are nearly identical, with only a minor divergence, demonstrating that the NPCMs are extremely thermally stable.

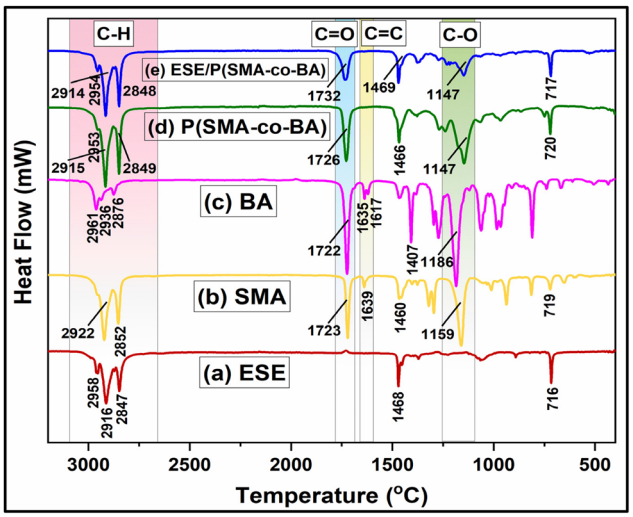

Fig. 7 FTIR spectra of ESE, SMA, BA, P(SMA-*co*-BA) and ESE/P(SMA-*co*-BA).

4.4. Diffusion-oozing circle test of the synthesized ESE/P (SMA-*co*-BA) nanocapsules

The diffusion-oozing circle test was utilized to evaluate the stability of the nanocapsules.[24,50] The nanocapsules were positioned on filter paper and maintained in an oven at 60 °C for 3 h. Subsequent to this interval, the magnitude of sample leakage was quantified as a percentage of the test area. Fig. 6 depicts the initial conditions of ESE and ESE/P(SMA-*co*-BA). Following 3 h of heating at 60 °C, the ESE became liquefied, whereas ESE/P(SMA-*co*-BA) maintained its structural integrity, with no leakage detected on the associated filter paper. The results demonstrate that the nanocapsules possess exceptional thermal stability.

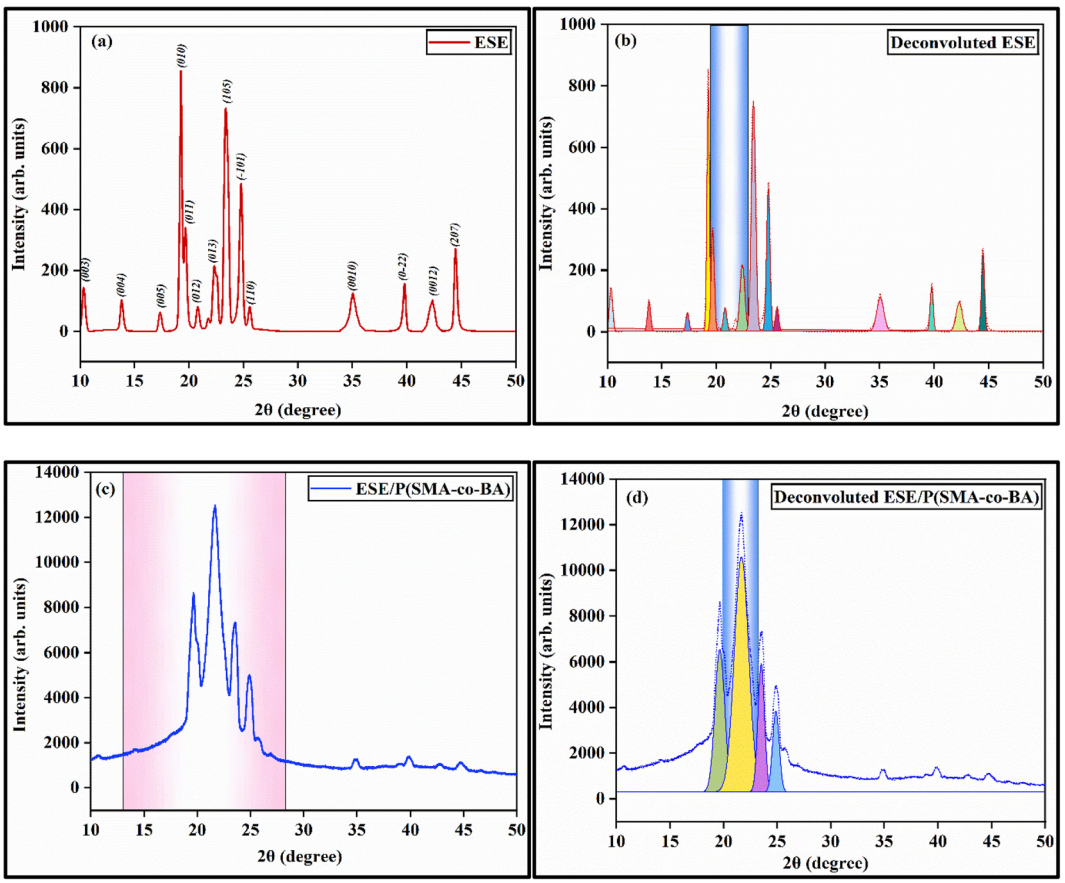

Fig. 8 PXRD pattern of (a) ESE, (b) deconvoluted ESE, (c) ESE/P(SMA-*co*-BA) and (d) deconvoluted ESE/P(SMA-*co*-BA).

4.5. FT-IR analysis of ESE/P(SMA-*co*-BA) nanocapsules

Fig. 7 presents the FTIR spectra of ESE, SMA, BA, P(SMA-*co*-BA) and ESE/P(SMA-*co*-BA) nanocapsules. Fig. 7(a) illustrates the ESE spectrum, which exhibits prominent peaks corresponding to the stretching vibration bands of C–H bonds in methyl and methylene groups at 2958 cm^{-1}, 2916 cm^{-1}, and 2847 cm^{-1}, respectively. The C–H bending vibration is observed at 1468 cm^{-1}, whereas the in-plane rocking vibration of the methylene group is associated with the peak at 716 cm^{-1}.[24] Fig. 7(b) depicts the FTIR spectrum of SMA, which is dominated by symmetric and asymmetric stretching vibrations of the long ester side groups. The bands at 2922 cm^{-1} and 2852 cm^{-1} correspond to the asymmetric and symmetric stretching vibrations of $-CH_3$ and $-CH_2$, respectively. The prominent band at 1723 cm^{-1} is attributed to the C=O stretching vibration, whereas the peak at 1460 cm^{-1} is associated with the bending vibration of $-CH_2$ groups. Additionally, the peak at 1159 cm^{-1} indicates C–O–C bond vibrations inside the ester group. The characteristic absorption peak at 719 cm^{-1} is ascribed to the extended carbon chain alkyl group [$-(CH_2)n-$, $n > 4$] in SMA.[35,45,51] The FTIR spectrum of BA, seen in Fig. 7(c), exhibits absorption peaks at 2961 cm^{-1}, 2936 cm^{-1}, and 2876 cm^{-1} corresponding to C–H stretching vibrations. The peak at 1722 cm^{-1} is attributed to C=O stretching, whereas the peaks at 1635 cm^{-1} and 1617 cm^{-1} are associated with C=C stretching. Furthermore, the peak at 1186 cm^{-1} represents C–O stretching vibrations, characteristic of the BA molecule.[52–54] Fig. 7(d) presents the FTIR spectrum of the polymer shell and shows the absence of a C=C absorption peak, which is observed in SMA and BA, confirming that both SMA and BA participated in the polymerization process. The spectrum of the synthesized nanocapsules [Fig. 7(e)] includes overlapping C–H stretching peaks of P(SMA-*co*-BA) and ESE, along with predominant peaks of SMA and BA, such as the 1732 cm^{-1} (C=O stretching) and 1147 cm^{-1} (C–O stretching) peaks. Additionally, the absence of the C=C absorption peak confirms that SMA and BA have successfully participated in the formation of ESE/P(SMA-*co*-BA).[55]

4.6. PXRD analysis of ESE/P(SMA-*co*-BA) nanocapsules

The PXRD patterns of ESE and ESE/P(SMA-*co*-BA) are displayed in Fig. 8(a) and (c). According to Varshney *et al.*,[24] the XRD analysis of ESE shows significant diffraction peaks with various 2θ values that precisely coincide with those listed in the 45-1543 standard PDF card No. This demonstrates that in the solid state, pure ESE has a distinct triclinic crystal structure.

The pristine ESE was enclosed within a polymer shell of SMA and a co-polymer shell of BA. The XRD pattern of ESE/P(SMA-*co*-BA) nanocapsules exhibits all the prevalent peaks corresponding to the highly ordered triclinic phase of ESE, as shown in Fig. 8(c). A notable peak at 21.6°, associated with a *d*-spacing of 0.4 nm in the crystal lattice, was observed. This peak is ascribed to the crystalline configuration of the elongated alkyl chain produced by the SMA polymer shell.[56–58] The appearance of this pronounced peak indicates the presence of a metastable face-centered orthorhombic rotator phase, linked to surface freezing phenomena often observed in *n*-alkanes within nanoscale structures.[59,60] The literature confirmed that the co-polymer BA shell exhibits a diffraction hump, indicating that the sample is amorphous.[61,62] In this study, a similar diffraction hump was observed in the range of 13–28°, thus confirming the presence of BA in the shell.

For a quantitative analysis, the deconvolution of the X-ray spectra for ESE and ESE/P(SMA-*co*-BA) is illustrated in Fig. 8(b) and (d). The deconvolution was executed by fitting a superposition of Gaussian functions to determine the integrated peak areas and refine the peak positions. In the deconvoluted ESE spectra, three sharp peaks were observed at 2θ values of 19.8, 20.8 and 22.4°, whereas in the deconvoluted ESE/P(SMA-*co*-BA) spectra, these three peaks were overlapped by the single crystalline peak at 21.6°, covering the area within the range of 19.5–23.9°. This may be attributed to chemical interactions between the core and the shell.

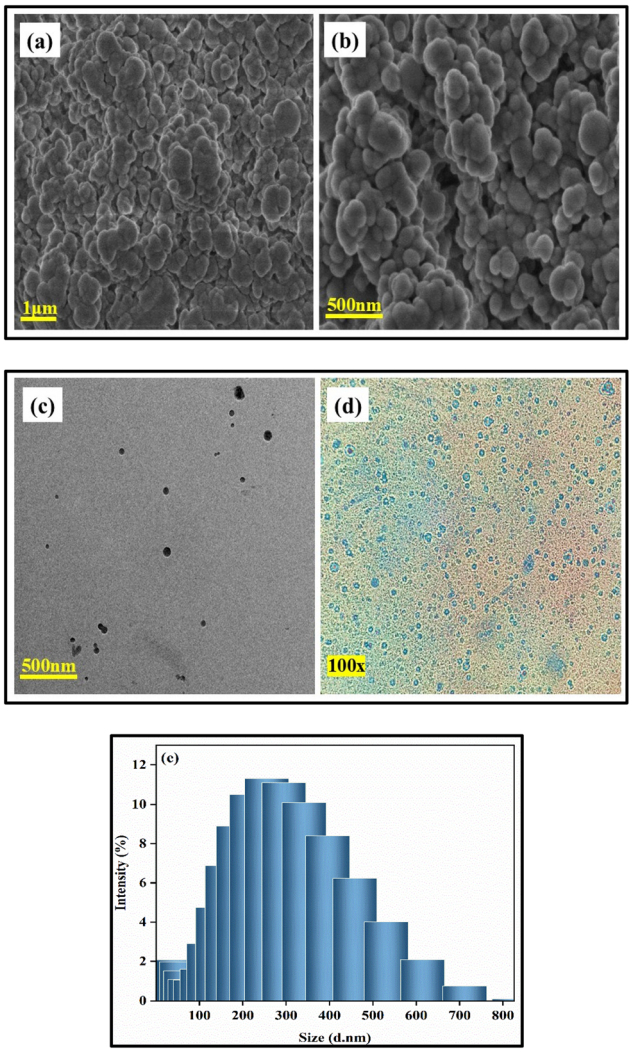

Fig. 9 (a) & (b) SEM micrographs, (c) TEM micrograph, (d) POM image and (e) PSD of the synthesized ESE/P(SMA-*co*-BA).

4.7. Morphological and PSD analysis of the synthesized NPCMs

The morphology and particle size of the produced ESE/P(SMA-*co*-BA) nanocapsules were examined using SEM, TEM, POM, and PSD analytical techniques. The acquired SEM/TEM micrographs and POM pictures are displayed in Fig. 9(a–d). The micrographs reveal that the nanocapsules have a spherical morphology with a slightly rough and non-uniform exterior surface. The SEM images indicate that certain regions of the capsules exhibit clustered formations. Conversely, similar structural types were not observed in TEM and POM images, as the particles were dispersed in an aqueous medium before the investigation. Furthermore, based on the scales shown on the SEM, TEM, and POM micrographs, it is clear that the synthesized NPCM was primarily composed of nano-spheres. Consequently, this nano-structured configuration can provide an increased surface area, thereby enhancing the heat transfer rate in latent heat TES systems.[40,63]

The PSD analysis results (Fig. 9e) indicate that the synthesized nanocapsules exhibit multimodal particle size distributions ranging from 0.4 to 825 nm. Furthermore, the average particle size was determined to be 195.3 nm. The particle size was also determined using ImageJ software, and the results were consistent with the PSD data.

5. Conclusions

The ESE/P(SMA-*co*-BA) nanocapsules, consisting of ESE as the core encapsulated within a P(SMA-*co*-BA) shell, have been developed using the mini-emulsion polymerization technique. The prepared ESE/P(SMA-*co*-BA) nanocapsules were examined utilizing various characterisation techniques. The fabricated ESE/P(SMA-*co*-BA) may serve as a latent heat TES material, as proven by the DSC results, with 87.2% E_{ES}, 93.6% E_R and 93.1% C_{es}. The melting and crystallisation temperatures of the synthesized nanocapsules are 37.4 °C and 25.1 °C, respectively, and the corresponding latent heat is 224.6 J g^{-1} and 191.7 J g^{-1}. According to the TGA study, the synthesized ESE/P(SMA-*co*-BA) nanocapsules have good thermal stability and degrade in two steps. FTIR results have confirmed that the prepared ESE/P(SMA-*co*-BA) nanocapsules contain all the characteristic peaks of ESE and P(SMA-*co*-BA). The PXRD patterns of the synthesized NPCMs exhibit all characteristic crystalline peaks of ESE. Additionally, the distinct peak at 21.6° signifies the crystalline structure of the long alkyl SMA polymer shell, while the diffraction hump reflects the amorphous nature of the copolymer shell. The SEM/TEM and POM analyses demonstrated that the produced nanocapsules have a fully spherical morphology, with some clustered formations featuring a rough exterior surface. The PSD study indicated that the diameters of the produced nanocapsules ranged from 0.4 to 825 nm, with a mean diameter of 195.3 nm. The synthesized ESE/P(SMA-*co*-BA) may be efficiently utilized for TES by incorporating it into various sectors, including electronic cooling, the food and textile industries, HVAC systems, cold-chain management, medicinal applications, and greenhouses to provide optimal conditions for plant development.

Author contributions

Gunjan Varshney: writing – original draft, methodology, investigation, formal analysis, data curation, and conceptualization. Raminder Kaur: writing – review & editing, validation, supervision, project administration, methodology, and conceptualization. Mohammad Zulfequar: validation and supervision.

Conflicts of interest

The work submitted in this manuscript has been conducted for research purposes only, and there is no conflict of interest involved.

Data availability

Raw Data of Differential Scanning Calorimetry (DSC), Thermo-Gravimetry Analysis (TGA), Derivative thermogravimetric analysis (DTG), Fourier Transform Infrared Spectroscopy (FT-IR) and Powder X-Ray Diffraction (XRD) are available at Harvard Dataverse at https://doi.org/10.7910/DVN/IECGC9.

Acknowledgements

We are thankful to Delhi Technological University for providing the necessary facilities to conduct this study.

References

1 S. Tanwar and R. Kaur, *Int. J. Energy Res.*, 2021, **45**, 17302–17314.
2 S. Tanwar and R. Kaur, *Energy Storage*, 2024, **6**, 1–11.
3 K. Yuan, J. Shi, W. Aftab, M. Qin, A. Usman, F. Zhou, Y. Lv, S. Gao and R. Zou, *Adv. Funct. Mater.*, 2020, **30**, 1904228.
4 S. Tanwar and R. Kaur, *J. Energy Storage*, 2022, **54**, 105318.
5 P. Ping, X. Dai, D. Kong, Y. Zhang, H. Zhao, X. Gao and W. Gao, *Chem. Eng. J.*, 2023, **463**, 142401.
6 G. Varshney, P. Singh, S. Yadav and R. Kaur, *Sustain. Energy Technol. Assessments*, 2024, **72**, 104089.
7 H. Yuan, S. Liu, S. Hao, Z. Zhang, H. An, W. Tian, M. Chan and H. Bai, *Sol. Energy Mater. Sol. Cells*, 2022, **239**, 111653.
8 H. Peng, J. Wang, X. Zhang, J. Ma, T. Shen, S. Li and B. Dong, *Appl. Therm. Eng.*, 2021, **185**, 116326.
9 J. Dhayanithi and T. K. Hotta, *Energy Built Environ.*, 2025, **6**, 796–808.
10 X. Chen, X. Huang, T.-Y. Shi, J.-X. Wang, X.-R. Yuan, H. Huang, J. Wang, R. He and X.-F. Yu, *ACS Omega*, 2022, **7**, 14952–14960.

11 R. Sattar, T. Ishaq, A. Afzal, R. Mukhtar and A. Naz, *Energy Sources, Part A*, 2022, **44**, 2133–2152.
12 S. Tanwar and R. Kaur, *Energy Storage*, 2024, **6**, e581.
13 S. Tanwar and R. Kaur, *Acad. Mater. Sci.*, 2024, **1**, 1–19.
14 Y. Huang, A. Stonehouse and C. Abeykoon, *Int. J. Heat Mass Transfer*, 2023, **200**, 123458.
15 A. Kumar, H. Jain and B. P. Tripathi, *ACS Appl. Energy Mater.*, 2020, **3**, 5965–5976.
16 H. Nikpourian, A. R. Bahramian and M. Abdollahi, Springer International Publishing, 2020, pp. 197–200.
17 N. Zhang and Y. Yuan, *Energy Built Environ.*, 2020, **1**, 410–416.
18 M. Ghulam, J. Z and Q. Wei, *J. Text. Sci. Eng.*, DOI: 10.4172/2165-8064.1000292.
19 A. Sarı, C. Alkan and C. Bilgin, *Appl. Energy*, 2014, **136**, 217–227.
20 J. Zhou, J. Zhao, Y. Cui and W. Cheng, *Polym. Int.*, 2020, **69**, 140–148.
21 M. Rezvanpour, M. Hasanzadeh, D. Azizi, A. Rezvanpour and M. Alizadeh, *Mater. Chem. Phys.*, 2018, **215**, 299–304.
22 M. Nikoonahad, S. M. Sadrameli and F. Arabpour Roghabadi, *J. Therm. Anal. Calorim.*, 2023, **148**, 10735–10747.
23 W. Lan, B. Shang, R. Wu, X. Yu, R. Hu and X. Luo, *Int. J. Therm. Sci.*, 2021, **159**, 106619.
24 G. Varshney, R. Kaur and M. Zulfequar, *Chem. Eng. J.*, 2024, **500**, 156994.
25 K. Tumirah, M. Z. Hussein, Z. Zulkarnain and R. Rafeadah, *Energy*, 2014, **66**, 881–890.
26 A. Sarı and A. Karaipekli, *Mater. Chem. Phys.*, 2008, **109**, 459–464.
27 C. Alkan, A. Sari, A. Karaipekli and O. Uzun, *Sol. Energy Mater. Sol. Cells*, 2009, **93**, 143–147.
28 S. Tahan Latibari, M. Mehrali, M. Mehrali, T. M. Indra Mahlia and H. S. Cornelis Metselaar, *Energy*, 2013, **61**, 664–672.
29 P. Sahu, A. K. Bhowmick and G. Kali, *Processes*, 2020, **8**, 553.
30 H. Tokuyama, R. Iriki and M. Kubota, *Gels*, 2023, **9**, 54.
31 H. Tokuyama and Y. Kato, *Eur. Polym. J.*, 2010, **46**, 277–282.
32 S. Li, H. Wang, L. Liu, H. Xu and H. Shi, *CrystEngComm*, 2018, **20**, 7348–7356.
33 P. J. Saikia, A. Goswami and S. D. Baruah, *J. Appl. Polym. Sci.*, 2002, **85**, 1236–1245.
34 X. Qiu, L. Lu, Z. Zhang, G. Tang and G. Song, *J. Therm. Anal. Calorim.*, 2014, **118**, 1441–1449.
35 B. Oktay, E. Baştürk, M. V. Kahraman and N. K. Apohan, *ChemistrySelect*, 2019, **4**, 5110–5115.
36 Y. Cao, D. Fan, S. Lin, L. Mu, F. T. T. Ng and Q. Pan, *Chem. Eng. J.*, 2020, **389**, 124318.
37 P. Sarkar and A. K. Bhowmick, *J. Polym. Sci., Part A: Polym. Chem.*, 2017, **55**, 2639–2649.
38 J. Shi, X. Wu, R. Sun, B. Ban, J. Li and J. Chen, *Mater. Chem. Phys.*, 2019, **231**, 244–251.
39 J. Shi, X. Wu, X. Fu and R. Sun, *Thermochim. Acta*, 2015, **617**, 90–94.
40 A. Sarı, C. Alkan, A. Biçer, A. Altuntaş and C. Bilgin, *Energy Convers. Manage.*, 2014, **86**, 614–621.
41 Y. Ma, Q. Xie, X. Wang and J. Lu, *Sol. Energy*, 2019, **179**, 410–423.
42 X. Qiu, L. Lu, J. Wang, G. Tang and G. Song, *Sol. Energy Mater. Sol. Cells*, 2014, **128**, 102–111.
43 X. Qiu, G. Song, X. Chu, X. Li and G. Tang, *Thermochim. Acta*, 2013, **551**, 136–144.
44 X. Qiu, L. Lu, G. Tang and G. Song, *J. Therm. Anal. Calorim.*, 2021, **143**, 3023–3032.
45 X. Qiu, L. Lu, J. Wang, G. Tang and G. Song, *Thermochim. Acta*, 2015, **620**, 10–17.
46 X. Qiu and L. Lu, *J. Renewable Sustainable Energy*, 2021, **13**, 14104.
47 F. He, X. Wang and D. Wu, *Energy*, 2014, **67**, 223–233.
48 H. Zhang, X. Wang and D. Wu, *J. Colloid Interface Sci.*, 2010, **343**, 246–255.
49 J. Y. Do, N. Son, J. Shin, R. K. Chava, S. W. Joo and M. Kang, *Mater. Des.*, 2021, **198**, 109357.
50 B. Ma, S. Adhikari, Y. Chang, J. Ren, J. Liu and Z. You, *Constr. Build. Mater.*, 2013, **42**, 114–121.
51 S. Mumby, J. D. Swalen and J. F. Rabolt, *Macromolecules*, 1986, **19**, 1054–1059.
52 A. Siddiq, M. Ghobashy, A.-B. El-Adasy and A. Ashmawy, *Sci. Rep.*, 2024, **14**, 8863.
53 M. Sultan, K. M. Zia, H. N. Bhatti, T. Jamil, R. Hussain and M. Zuber, *Carbohydr. Polym.*, 2012, **87**, 397–404.
54 Z. Sheng, J. Wang and S. Song, *J. Mater. Sci.*, 2020, **55**, 11739–11751.
55 X. Zhao and C. Fang, *Int. J. Adhes. Adhes.*, 2024, **135**, 103848.
56 B. Elarbe, I. Elganidi, N. Ridzuan, K. Yusoh, N. Abdullah and S. Vijayakumar, *J. Pet. Explor. Prod. Technol.*, 2022, **12**, 1811–1828.
57 C. Xiao, X. Yin, J. Chen, Y. Wang, W. Liao, J. Zhang, W. Jiang and C. Tu, *J. Appl. Polym. Sci.*, 2024, **141**, e55876.
58 P. P. Dutta, B. Mohan and P. J. Saikia, *Ind. Eng. Chem. Res.*, 2024, **63**, 10879–10891.
59 H. Park, C. Kwak, J. Lee, S. Lim, J. Yang, J. Kim, S. Y. Ryu, H. Bin Na and J. Lee, *ACS Appl. Mater. Interfaces*, 2020, **12**, 51092–51101.
60 P. F. De Castro, A. Ahmed and D. G. Shchukin, *Chem. – Eur. J.*, 2016, **22**, 4389–4394.
61 C. Ma, Q. Liang, C. Kou, H. Zhang and H. Wang, *Polym. Sci., Ser. B*, 2022, **64**, 725–732.
62 K. Matsuura, K. Kuboyama and T. Ougizawa, *J. Appl. Polym. Sci.*, 2021, **138**, 50268.
63 A. Sarı, C. Alkan, D. Kahraman Döğüşcü and A. Biçer, *Sol. Energy Mater. Sol. Cells*, 2014, **126**, 42–50.